Residual Stream Analysis with Multi-Layer SAEs

Tim Lawson[*] **Lucy Farnik** **Conor Houghton** **Laurence Aitchison**
School of Engineering Mathematics and Technology
University of Bristol
Bristol, UK

Abstract

Sparse autoencoders (SAEs) are a promising approach to interpreting the internal representations of transformer language models. However, SAEs are usually trained separately on each transformer layer, making it difficult to use them to study how information flows across layers. To solve this problem, we introduce the multi-layer SAE (MLSAE): a single SAE trained on the residual stream activation vectors from every transformer layer. Given that the residual stream is understood to preserve information across layers, we expected MLSAE latents to 'switch on' at a token position and remain active at later layers. Interestingly, we find that individual latents are often active at a single layer for a given token or prompt, but the layer at which an individual latent is active may differ for different tokens or prompts. We quantify these phenomena by defining a distribution over layers and considering its variance. We find that the variance of the distributions of latent activations over layers is about two orders of magnitude greater when aggregating over tokens compared with a single token. For larger underlying models, the degree to which latents are active at multiple layers increases, which is consistent with the fact that the residual stream activation vectors at adjacent layers become more similar. Our results represent a new approach to understanding how representations change as they flow through transformers. We release our code to train and analyze MLSAEs at `https://github.com/tim-lawson/mlsae`.

1 Introduction

Sparse autoencoders (SAEs) learn interpretable directions or 'features' in the representation spaces of language models (Elhage et al., 2022; Cunningham et al., 2023; Bricken et al., 2023). Typically, SAEs are trained on the activation vectors from a single model layer (Gao et al., 2024; Templeton et al., 2024; Lieberum et al., 2024). This approach illuminates the representations within a layer. However, Olah (2024); Templeton et al. (2024) believe that models may encode meaningful concepts by simultaneous activations in multiple layers, which SAEs trained at a single layer do not address. Furthermore, it is not straightforward to automatically identify correspondences between features from SAEs trained at different layers, which may complicate circuit analysis (e.g. He et al., 2024).

To solve this problem, we take inspiration from the residual stream perspective, which states that transformers (Vaswani et al., 2017) selectively write information to and read information from token positions with self-attention and MLP layers (Elhage et al., 2021; Ferrando et al., 2024). The results of subsequent circuit analyses, like the explanation of the indirect object identification task presented by Wang et al. (2022), support this viewpoint and cause us to expect the activation vectors at adjacent layers in the residual stream to be relatively similar (Lad et al., 2024).

To capture the structure shared between layers in the residual stream, we introduce the multi-layer SAE (MLSAE): a single SAE trained on the residual stream activation vectors from every layer of

[*]Correspondence to `tim.lawson@bristol.ac.uk`.

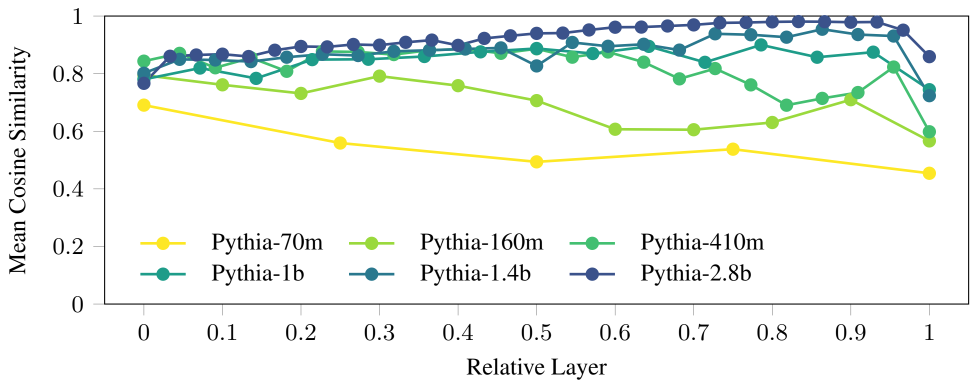

Figure 1: The mean cosine similarities between the residual stream activation vectors at adjacent layers of transformers, over 10 million tokens from the test set. To compare transformers with different numbers of layers, we divide the lower of each pair of adjacent layers by the number of pairs. This 'relative layer' is the x-axis of the plot. We subtract the dataset mean from the activation vectors at each layer before computing cosine similarities to control for changes in the norm between layers (Heimersheim & Turner, 2023), which we demonstrate in Figure 4.

a transformer language model. Importantly, the autoencoder itself has a single hidden layer – it is multi-layer only in the sense that it is trained on activations from multiple layers of the underlying transformer. In particular, we consider the activation vectors from each layer as separate training examples, which is equivalent to training a single SAE at each layer individually but with the parameters tied across layers. We briefly discuss alternative methods in Section 5.

We show that multi-layer SAEs achieve comparable reconstruction error and downstream loss to single-layer SAEs (Appendix C) while allowing us to directly identify and analyze features that are active at multiple layers. When aggregating over a large sample of tokens, we find that individual latents are likely to be active at multiple layers, and this measure increases with the number of latents. However, for a single token, latent activations are more likely to be isolated to a single layer. For larger underlying transformers, we show that the residual stream activation vectors at adjacent layers are more similar and that the degree to which latents are active at multiple layers increases.

2 Related work

A sparse code represents many signals, such as sensory inputs, by simultaneously activating a relatively small number of elements, such as neurons (Bell & Sejnowski, 1995; Olshausen & Field, 1996). Sparse dictionary learning (SDL) approximates each input vector by a linear combination of a relatively small number of learned basis vectors. The learned basis is usually overcomplete: it has a greater dimension than the inputs. SDL algorithms include Independent Component Analysis (Bell & Sejnowski, 1997; Hyvärinen & Oja, 2000; Le et al., 2011) and sparse autoencoders (Lee et al., 2006; Ng, 2011; Makhzani & Frey, 2014).

The activations of language models have been hypothesized to be a dense, compressed version of a sparse, expanded representation space (Elhage et al., 2021, 2022). Under this view, there are interpretable directions in the dense representation spaces corresponding to distinct semantic concepts, whereas their basis vectors (neurons) are 'polysemantic' (Park et al., 2023). It has been shown theoretically (Wright & Ma, 2022) and empirically (Elhage et al., 2022; Sharkey et al., 2022; Whittington et al., 2023) that SDL recovers ground-truth features in toy models, and that learned dictionary elements are more interpretable than the basis vectors of language models (Cunningham et al., 2023; Bricken et al., 2023) or dense embeddings (O'Neill et al., 2024). Notably, features are not necessarily linear (Wattenberg & Viégas, 2024; Engels et al., 2024; Hernandez et al., 2024).

The standard SAE architecture is a single hidden layer with a ReLU activation function and an L^1 sparsity penalty in the training loss (Bricken et al., 2023), but various activation functions (Makhzani & Frey, 2014; Konda et al., 2015; Rajamanoharan et al., 2024b,a) and objectives (Braun et al., 2024) have been proposed. The prevailing approach is to train an SAE on the activation vectors from a

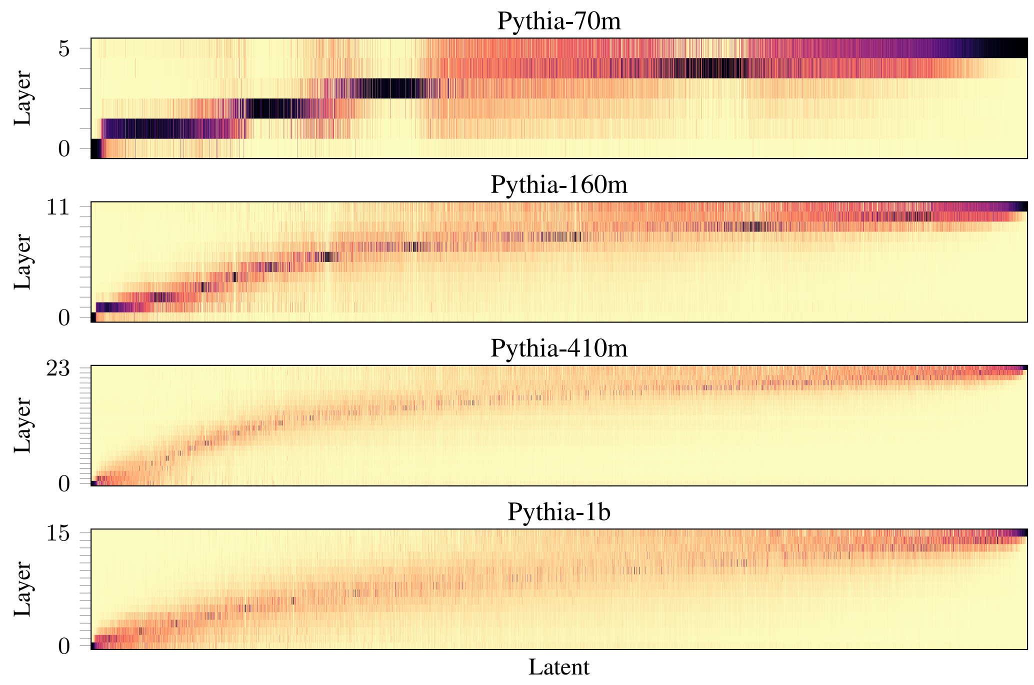

Figure 2: Heatmaps of the distributions of latent activations over layers when aggregating over 10 million tokens from the test set. Here, we plot the distributions for MLSAEs trained on Pythia models with an expansion factor of $R = 64$ and sparsity $k = 32$. The latents are sorted in ascending order of the expected value of the layer index (Equation 6).

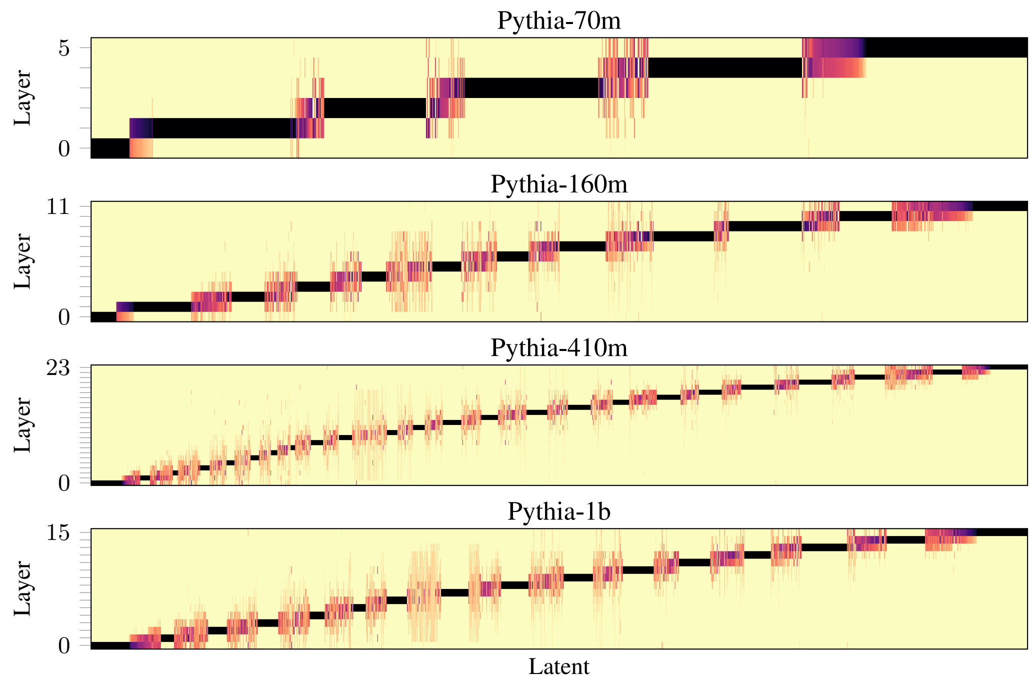

Figure 3: Heatmaps of the distributions of latent activations over layers for a single example prompt. Here, we plot the distributions for MLSAEs trained on Pythia models with an expansion factor of $R = 64$ and sparsity $k = 32$. The example prompt is "When John and Mary went to the store, John gave" (Wang et al., 2022). We exclude latents with maximum activation below 1×10^{-3} and sort latents in ascending order of the expected value of the layer index (Equation 6).

single transformer layer, except for Kissane et al. (2024), who concatenate the outputs of multiple attention heads in a single layer, and Yun et al. (2021), who learn an undercomplete basis for the residual stream at multiple layers, albeit by iterative optimization instead of with an autoencoder.

Mechanistic interpretability research often attempts to identify circuits: computational subgraphs of neural networks that implement specific behaviors (Olah et al., 2020; Wang et al., 2022; Conmy et al., 2023; Dunefsky et al., 2024; García-Carrasco et al., 2024; Marks et al., 2024). Representing networks in terms of SAE latents may help to improve circuit discovery (He et al., 2024; O'Neill & Bui, 2024), and these latents can be used to construct steering vectors (Subramani et al., 2022; Templeton et al., 2024; Makelov, 2024), but it is unclear whether SAEs outperform baselines for causal analysis (Chaudhary & Geiger, 2024; Huang et al., 2024). Importantly, SAEs can be scaled up to the activations of large language models, where we expect the number of distinct semantic concepts to be extremely large (Templeton et al., 2024; Gao et al., 2024; Lieberum et al., 2024).

The key difference between previous work (Bricken et al., 2023; Cunningham et al., 2023; Templeton et al., 2024; Gao et al., 2024) and our work is that we introduce the multi-layer SAE, i.e., we train a single SAE at all layers of the residual stream.

3 Methods

The key idea with a multi-layer SAE is to train a single SAE on the residual stream activation vectors from every layer. In particular, we consider the activations at each layer to be different training examples. Hence, for residual stream activation vectors of model dimension d, the inputs to the multi-layer SAE also have dimension d. For n_T tokens and n_L layers, we train the multi-layer SAE on $n_T n_L$ activation vectors. We use the terms 'SAE feature' and 'latent' interchangeably.

3.1 Setup

We train MLSAEs on GPT-style language models from the Pythia suite (Biderman et al., 2023). We are primarily interested in the computation performed by self-attention and MLP layers on intermediate representations (Valeriani et al., 2023), so we exclude the input embeddings before the first transformer block and take the last-layer activations before the final layer norm.

We use a k-sparse autoencoder (Makhzani & Frey, 2014; Gao et al., 2024), which directly controls the sparsity of the latent space by introducing a TopK activation function that keeps only the k largest latents. The k largest latents are almost always positive for $k \ll d$, but we follow Gao et al. (2024) in applying a ReLU activation function to guarantee non-negativity. This setup effectively fixes the sparsity (L^0 norm) of the latents at k per activation vector (layer and token) throughout training. For input vectors $\mathbf{x} \in \mathbb{R}^d$ and latent vectors $\mathbf{h} \in \mathbb{R}^n$, the encoder and decoder are defined by:

$$\mathbf{h} = \mathrm{ReLU}(\mathrm{TopK}(\mathbf{W}_{\text{enc}}\mathbf{x} - \mathbf{b}_{\text{pre}})) \ , \quad \hat{\mathbf{x}} = \mathbf{W}_{\text{dec}}\mathbf{h} + \mathbf{b}_{\text{pre}} \tag{1}$$

where $\mathbf{W}_{\text{enc}} \in \mathbb{R}^{d \times n}$, $\mathbf{W}_{\text{dec}} \in \mathbb{R}^{n \times d}$, and $\mathbf{b}_{\text{pre}} \in \mathbb{R}^d$. We constrain the pre-encoder bias $\mathbf{b}_{\text{pre}}$ to be the negative of the post-decoder bias, following Bricken et al. (2023); Gao et al. (2024), and standardize activation vectors to zero mean and unit variance before passing them to the encoder.

3.2 Training

We use the fraction of variance unexplained (FVU) as the reconstruction error:

$$\mathrm{FVU}(\mathbf{x}, \hat{\mathbf{x}}) = \frac{1}{n_L} \sum_{\ell=0}^{n_L - 1} \frac{\|\mathbf{x}^{(\ell)} - \hat{\mathbf{x}}^{(\ell)}\|_2^2}{\mathrm{Var}(\mathbf{x}^{(\ell)})} \tag{2}$$

Here, Var is the variance. We chose the FVU because the input vectors from different layers may have different magnitudes; choosing the mean squared error (MSE) would encourage the autoencoder to prioritize minimizing the reconstruction errors of the layers with the greatest magnitudes.

A potential issue when training SAEs is the occurrence of 'dead' latents, i.e., latent dimensions that are almost always zero. With a k-sparse autoencoder, this means latent dimensions that almost never appear among the k largest latent activations. We follow Bricken et al. (2023); Cunningham et al. (2023) by considering a latent 'dead' if it is not activated within the last 10 million tokens during training. In the multi-layer setting, a latent may be activated by the input vectors from any layer.

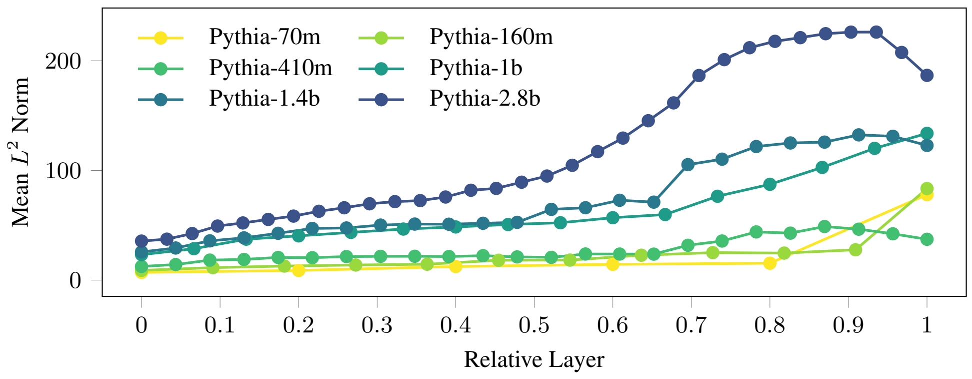

Figure 4: The mean L^2 norm of the residual stream activation vectors at every layer, over 10 million tokens from the test set. To compare transformers with different numbers of layers, we divide the layer index ℓ by the number of layers n_L. This 'relative layer' is the x-axis of the plot.

Gao et al. (2024, Appendix A.2) propose an auxiliary loss term to minimize the occurrence of dead latents. This AuxK term models the MSE reconstruction error using the k_{aux} largest dead latents:

$$\text{AuxK}(\mathbf{x}, \hat{\mathbf{x}}) = \|\mathbf{e} - \hat{\mathbf{e}}\|_2^2 \tag{3}$$

Here, $\mathbf{e} = \mathbf{x} - \hat{\mathbf{x}}$ is the reconstruction error of the main model, and $\hat{\mathbf{e}}$ is its reconstruction using the top-k_{aux} dead latents. Let Dead be an 'activation function' that keeps only the dead latents. Then:

$$\mathbf{h}_{\text{dead}} = \text{ReLU}(\text{TopK}_{\text{aux}}(\text{Dead}(\mathbf{W}_{\text{enc}}\mathbf{x} - \mathbf{b}_{\text{pre}}))) \ , \quad \hat{\mathbf{e}} = \mathbf{W}_{\text{dec}}\mathbf{h}_{\text{dead}} + \mathbf{b}_{\text{pre}} \tag{4}$$

The full loss is the FVU plus the auxiliary loss term, multiplied by a small coefficient α:

$$\mathcal{L} = \text{FVU}(\mathbf{x}, \hat{\mathbf{x}}) + \alpha \cdot \text{AuxK}(\mathbf{x}, \hat{\mathbf{x}}) \tag{5}$$

Following Gao et al. (2024), we choose k_{aux} as a power of 2 close to ${}^{d}/_{2}$ and $\alpha = {}^{1}/_{32}$.

Our hyperparameters are the expansion factor $R = {}^{n}/_{d}$, the ratio of the number of latents to the model dimension, and the sparsity k, the number of largest latents to keep in the TopK activation function. We choose expansion factors as powers of 2 between 1 and 256, yielding autoencoders with between 512 and 131072 latents for Pythia-70m, and k as powers of 2 between 16 and 512.

The implementation is based on Gao et al. (2023); Belrose (2024); see Appendix A for details.

4 Results

4.1 Representation drift

Guided by the residual stream perspective (Elhage et al., 2021; Ferrando et al., 2024), we expected dense activation vectors to be relatively similar across layers. As an approximate measure of the degree to which information is preserved in the residual stream, we computed the cosine similarities between the activation vectors at adjacent layers, similarly to Lad et al. (2024, Appendix A).

A similarity of one means that the information represented at a token position is unchanged by the intervening residual block, whereas a similarity of zero means the activation vectors on either side of the block are orthogonal. We had expected changes in the residual stream to become smaller as the model size increased, and we confirmed that the mean cosine similarities increased as the model size increased (Figure 1).

Given that the residual stream activation vectors are relatively similar between adjacent layers, we expected to find many MLSAE latents active at multiple layers. We confirmed this prediction over a large sample of 10 million tokens from the test set (Figure 2). Interestingly, we found that for individual prompts, a much greater proportion of latents are active at only a single layer (Figure 3).

Following Heimersheim & Turner (2023), we verified that the mean L^2 norm of the activation vectors increases across layers, which prompted us to center the vectors at each layer before computing the similarities between them (Figure 4).

4.2 Latent distributions over layers

Given a dataset and MLSAE, each combination of a token and latent produces a distribution of activations over layers. We want to understand the degree to which the variance of that distribution depends on the token versus the latent to quantify the intuition gleaned from Figures 2 and 3.

Consider the layer index L, token T, and latent index J to be random variables. We take $P(J)$ to be a uniform discrete distribution, $P(T \mid J)$ to be a uniform discrete distribution over tokens for which the latent is active (at any layer), and L to be sampled from a conditional distribution proportional to the total latent activation at that layer, aggregating over tokens:

$$P\left(L=\ell \mid T=t,\, J=j\right)=\frac{h_j(\mathbf{x}_t^{(\ell)})}{\sum_{\ell'} h_j(\mathbf{x}_t^{(\ell')})} \tag{6}$$

Here, $\mathbf{x}_t^{(\ell)}$ is the dense residual stream activation vector at token t and layer ℓ, while $h_j(\mathbf{x}_t^{(\ell)})$ is the activation of the j-th MLSAE latent at that token and layer. We order latents in all heatmaps using the expected value of the layer index for a single latent $\mathbb{E}_T[L \mid J=j]$.

The variance of the distribution over layers measures the degree to which a latent is active at a single layer (in which case, it is zero) versus multiple layers (in which case, it is positive). We are interested in the following variances of the distribution over layers:

- $\mathrm{Var}(L \mid J=j,\, T=t)$, for a single latent and token
- $\mathrm{Var}(L \mid J=j)$, for a single latent, aggregating over tokens
- $\mathrm{Var}(L)$, aggregating over both latents and tokens

These quantities are related by the law of total variance. For the moment, we note that the variance of the distribution over layers naturally depends on the number of layers n_L. Hence, to compare different models, we look at ratios between these variances:

$$\begin{array}{c} \text{variance for one latent, aggregating over tokens,} \\ \text{as a proportion of the total variance over all latents} \end{array} = \frac{\mathbb{E}_J[\mathrm{Var}(L \mid J)]}{\mathrm{Var}(L)} \tag{7}$$

$$\begin{array}{c} \text{variance for one token and latent as a} \\ \text{proportion of the total variance for that latent} \end{array} = \frac{\mathbb{E}_{J,T}[\mathrm{Var}(L \mid J,\, T)]}{\mathbb{E}_J[\mathrm{Var}(L \mid J)]} \tag{8}$$

The former measures the degree to which latents are active at multiple layers when aggregating over tokens, and the latter compares this to the case for a single token.

The degree to which latents are active at multiple layers when aggregating over tokens is relatively large, between 54 and 86%, and increases uniformly with the model size for fixed hyperparameters (Figure 5). This measure quantifies the observation that, in the aggregate heatmaps (Figure 2), the distributions of latent activations over layers become more 'spread out' as the model size increases. Conversely, we find that the fraction of the variance for an individual latent explained by individual tokens is very small, about 1%. This quantifies the observation that, in the single-prompt heatmaps (Figure 3), the distributions over layers are much less 'spread out' than in the aggregate heatmaps.

5 Discussion

We considered the activation vectors from different layers as different training examples, so we passed $n_L n_T$ vectors of length d to the autoencoder, where n_T is the number of tokens, n_L is the number of layers, and d is the dimension of the residual stream. This approach might be called a 'data-stacked' MLSAE. An alternative would be a 'feature-stacked' MLSAE, i.e., to concatenate the activation vectors from different layers into a single vector of dimension $n_L d$. This alternative might be better suited to capturing the notion of 'cross-layer superposition,' which we take to mean a small number of simultaneously active sparse features at multiple layers encoding a single meaningful concept (Olah, 2024; Templeton et al., 2024).

We began by pursuing the feature-stacked approach but discarded it. The essential issue is that a single set of sparse features describes the residual stream activations at every layer, which makes it difficult to understand how information flows through a transformer. For example, it would not be possible

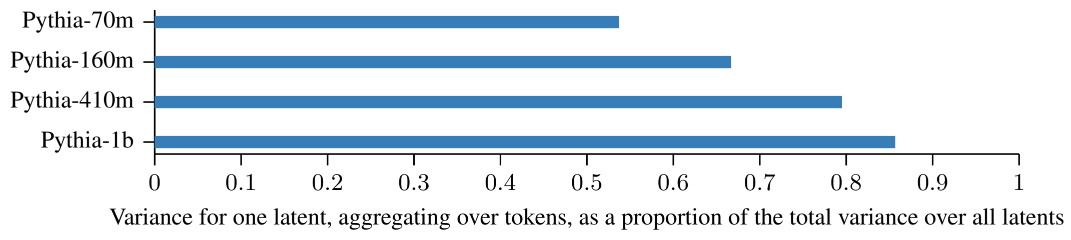

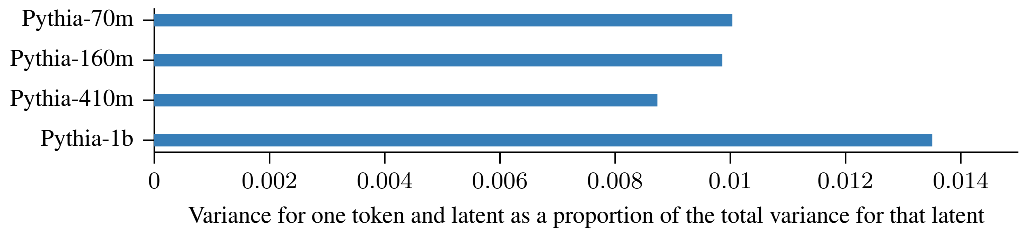

Figure 5: The fraction of the total variance explained by individual latents and the fraction of the variance for an individual latent explained by individual tokens (Equations 7 and 8) for MLSAEs with an expansion factor of $R = 64$ and sparsity $k = 32$, over 10 million tokens from the test set. For other hyperparameters, see Figure 16.

to plot the activations of sparse features across layers. Moreover, to compute this set of features, one must first compute the activations at every layer, which makes it more difficult to evaluate performance by traditional measures like single-layer reconstruction errors. Finally, the information encoded at one token position may differ substantially between layers due to self-attention. In the early layers, the representation is likely to primarily encode the input token and position embedding, whereas in the later layers, the representation may encode more complex properties of the surrounding context. It is not immediately apparent that jointly encoding this information by a single SAE is sensible. Instead, one might wish to separately capture the different information present at a token position across layers, which is allowed with our data-stacked approach.

6 Conclusion

We introduced the multi-layer SAE (MLSAE), where we train a single SAE on the activations at every layer of the residual stream. This allowed us to study both how information is represented within a single transformer layer and how information flows through the residual stream.

We confirmed that residual stream activations are relatively similar across layers by looking at cosine similarities before considering the distributions of latent activations over layers. When aggregating over a large sample of ten million tokens, we observed that most latents were active at multiple layers, but for a single prompt, most latent activations were isolated to a single layer. To quantify these observations, we computed the fraction of the total variance explained by individual latents and the fraction of the variance for an individual latent explained by individual tokens. This analysis confirmed that the degree to which latents are active at multiple layers when aggregating over tokens was large, increasing with the model size and expansion factor, and that the fraction of the variance explained by individual tokens was small.

Understanding how representations change as they flow through transformers is critical to identifying meaningful circuits, which is a core task of mechanistic interpretability. Despite the utility of the residual stream perspective, our results demonstrate that representation drift, and perhaps the increasing magnitude of changes to the residual stream across layers, is a significant obstacle to identifying meaningful computational variables with SAEs. Nevertheless, we argue that an approach such as the MLSAE, which considers the representations at multiple layers in parallel, is necessary for future methods that seek to interpret the internal computations of transformer language models.

References

Anthony J. Bell and Terrence J. Sejnowski. An Information-Maximization Approach to Blind Separation and Blind Deconvolution. *Neural Computation*, 7(6):1129–1159, November 1995. ISSN 0899-7667. doi: 10.1162/neco.1995.7.6.1129. URL https://ieeexplore.ieee.org/abstract/document/6796129. Conference Name: Neural Computation.

Anthony J. Bell and Terrence J. Sejnowski. The "independent components" of natural scenes are edge filters. *Vision Research*, 37(23):3327–3338, December 1997. ISSN 0042-6989. doi: 10.1016/S0042-6989(97)00121-1. URL https://www.sciencedirect.com/science/article/pii/S0042698997001211.

Nora Belrose. EleutherAI/sae, May 2024. URL https://github.com/EleutherAI/sae.

Nora Belrose, Zach Furman, Logan Smith, Danny Halawi, Igor Ostrovsky, Lev McKinney, Stella Biderman, and Jacob Steinhardt. Eliciting Latent Predictions from Transformers with the Tuned Lens, November 2023. URL http://arxiv.org/abs/2303.08112. arXiv:2303.08112 [cs].

Stella Biderman, Hailey Schoelkopf, Quentin Gregory Anthony, Herbie Bradley, Kyle O'Brien, Eric Hallahan, Mohammad Aflah Khan, Shivanshu Purohit, Usvsn Sai Prashanth, Edward Raff, Aviya Skowron, Lintang Sutawika, and Oskar Van Der Wal. Pythia: A Suite for Analyzing Large Language Models Across Training and Scaling. In *Proceedings of the 40th International Conference on Machine Learning*, pp. 2397–2430. PMLR, July 2023. URL https://proceedings.mlr.press/v202/biderman23a.html. ISSN: 2640-3498.

Dan Braun, Jordan Taylor, Nicholas Goldowsky-Dill, and Lee Sharkey. Identifying Functionally Important Features with End-to-End Sparse Dictionary Learning, May 2024. URL http://arxiv.org/abs/2405.12241. arXiv:2405.12241 [cs].

Trenton Bricken, Adly Templeton, Joshua Batson, Brian Chen, Adam Jermyn, Tom Conerly, Nick Turner, Cem Anil, Carson Denison, and Amanda Askell. Towards Monosemanticity: Decomposing Language Models With Dictionary Learning, 2023. URL https://transformer-circuits.pub/2023/monosemantic-features.

Maheep Chaudhary and Atticus Geiger. Evaluating Open-Source Sparse Autoencoders on Disentangling Factual Knowledge in GPT-2 Small, September 2024. URL http://arxiv.org/abs/2409.04478. arXiv:2409.04478 [cs].

Arthur Conmy, Augustine Mavor-Parker, Aengus Lynch, Stefan Heimersheim, and Adrià Garriga-Alonso. Towards Automated Circuit Discovery for Mechanistic Interpretability. *Advances in Neural Information Processing Systems*, 36:16318–16352, December 2023. URL https://proceedings.neurips.cc/paper_files/paper/2023/hash/34e1dbe95d34d7ebaf99b9bcaeb5b2be-Abstract-Conference.html.

Hoagy Cunningham, Aidan Ewart, Logan Riggs, Robert Huben, and Lee Sharkey. Sparse Autoencoders Find Highly Interpretable Features in Language Models, October 2023. URL http://arxiv.org/abs/2309.08600. arXiv:2309.08600 [cs].

Jacob Dunefsky, Philippe Chlenski, and Neel Nanda. Transcoders Find Interpretable LLM Feature Circuits, June 2024. URL http://arxiv.org/abs/2406.11944. arXiv:2406.11944 [cs].

Nelson Elhage, Neel Nanda, Catherine Olsson, T. Henighan, N. Joseph, B. Mann, A. Askell, Y. Bai, A. Chen, and T. Conerly. A Mathematical Framework for Transformer Circuits, 2021. URL https://transformer-circuits.pub/2021/framework/index.html.

Nelson Elhage, Tristan Hume, Catherine Olsson, Nicholas Schiefer, Tom Henighan, Shauna Kravec, Zac Hatfield-Dodds, Robert Lasenby, Dawn Drain, Carol Chen, Roger Grosse, Sam McCandlish, Jared Kaplan, Dario Amodei, Martin Wattenberg, and Christopher Olah. Toy Models of Superposition, September 2022. URL http://arxiv.org/abs/2209.10652. arXiv:2209.10652 [cs].

Joshua Engels, Isaac Liao, Eric J. Michaud, Wes Gurnee, and Max Tegmark. Not All Language Model Features Are Linear, May 2024. URL http://arxiv.org/abs/2405.14860. arXiv:2405.14860 [cs].

Javier Ferrando, Gabriele Sarti, Arianna Bisazza, and Marta R. Costa-jussà. A Primer on the Inner Workings of Transformer-based Language Models, May 2024. URL http://arxiv.org/abs/2405.00208. arXiv:2405.00208 [cs].

Leo Gao, Stella Biderman, Sid Black, Laurence Golding, Travis Hoppe, Charles Foster, Jason Phang, Horace He, Anish Thite, Noa Nabeshima, Shawn Presser, and Connor Leahy. The Pile: An 800GB Dataset of Diverse Text for Language Modeling, December 2020. URL http://arxiv.org/abs/2101.00027. arXiv:2101.00027 [cs].

Leo Gao, Tom Dupré la Tour, and Jeffrey Wu. openai/sparse_autoencoder, December 2023. URL https://github.com/openai/sparse_autoencoder.

Leo Gao, Tom Dupré la Tour, Henk Tillman, Gabriel Goh, Rajan Troll, Alec Radford, Ilya Sutskever, Jan Leike, and Jeffrey Wu. Scaling and evaluating sparse autoencoders, June 2024. URL http://arxiv.org/abs/2406.04093. arXiv:2406.04093 [cs].

Jorge García-Carrasco, Alejandro Maté, and Juan Carlos Trujillo. How does GPT-2 Predict Acronyms? Extracting and Understanding a Circuit via Mechanistic Interpretability. In *Proceedings of The 27th International Conference on Artificial Intelligence and Statistics*, pp. 3322–3330. PMLR, April 2024. URL https://proceedings.mlr.press/v238/garcia-carrasco24a.html. ISSN: 2640-3498.

Zhengfu He, Xuyang Ge, Qiong Tang, Tianxiang Sun, Qinyuan Cheng, and Xipeng Qiu. Dictionary Learning Improves Patch-Free Circuit Discovery in Mechanistic Interpretability: A Case Study on Othello-GPT, February 2024. URL http://arxiv.org/abs/2402.12201. arXiv:2402.12201 [cs].

Stefan Heimersheim and Alex Turner. Residual stream norms grow exponentially over the forward pass, May 2023. URL https://www.alignmentforum.org/posts/8mizBCm3dyc432nK8/residual-stream-norms-grow-exponentially-over-the-forward.

Evan Hernandez, Arnab Sen Sharma, Tal Haklay, Kevin Meng, Martin Wattenberg, Jacob Andreas, Yonatan Belinkov, and David Bau. Linearity of Relation Decoding in Transformer Language Models, February 2024. URL http://arxiv.org/abs/2308.09124. arXiv:2308.09124 [cs].

Jing Huang, Zhengxuan Wu, Christopher Potts, Mor Geva, and Atticus Geiger. RAVEL: Evaluating Interpretability Methods on Disentangling Language Model Representations, August 2024. URL http://arxiv.org/abs/2402.17700. arXiv:2402.17700 [cs].

A. Hyvärinen and E. Oja. Independent component analysis: algorithms and applications. *Neural Networks*, 13(4):411–430, June 2000. ISSN 0893-6080. doi: 10.1016/S0893-6080(00)00026-5. URL https://www.sciencedirect.com/science/article/pii/S0893608000000265.

Stanisław Jastrzębski, Devansh Arpit, Nicolas Ballas, Vikas Verma, Tong Che, and Yoshua Bengio. Residual Connections Encourage Iterative Inference, March 2018. URL http://arxiv.org/abs/1710.04773. arXiv:1710.04773 [cs].

Diederik P. Kingma and Jimmy Ba. Adam: A Method for Stochastic Optimization, January 2017. URL http://arxiv.org/abs/1412.6980. arXiv:1412.6980 [cs].

Connor Kissane, Robert Krzyzanowski, Joseph Isaac Bloom, Arthur Conmy, and Neel Nanda. Interpreting Attention Layer Outputs with Sparse Autoencoders. June 2024. URL https://openreview.net/forum?id=fewUBDwjji.

Kishore Konda, Roland Memisevic, and David Krueger. Zero-bias autoencoders and the benefits of co-adapting features, April 2015. URL http://arxiv.org/abs/1402.3337. arXiv:1402.3337 [cs, stat].

Vedang Lad, Wes Gurnee, and Max Tegmark. The Remarkable Robustness of LLMs: Stages of Inference?, June 2024. URL http://arxiv.org/abs/2406.19384. arXiv:2406.19384 [cs].

Quoc Le, Alexandre Karpenko, Jiquan Ngiam, and Andrew Ng. ICA with Reconstruction Cost for Efficient Overcomplete Feature Learning. In *Advances in Neural Information Processing Systems*, volume 24. Curran Associates, Inc., 2011. URL https://proceedings.neurips.cc/paper/2011/hash/233509073ed3432027d48b1a83f5fbd2-Abstract.html.

Honglak Lee, Alexis Battle, Rajat Raina, and Andrew Ng. Efficient sparse coding algorithms. In *Advances in Neural Information Processing Systems*, volume 19. MIT Press, 2006. URL https://proceedings.neurips.cc/paper_files/paper/2006/hash/2d71b2ae158c7c5912cc0bbde2bb9d95-Abstract.html.

Tom Lieberum, Senthooran Rajamanoharan, Arthur Conmy, Lewis Smith, Nicolas Sonnerat, Vikrant Varma, János Kramár, Anca Dragan, Rohin Shah, and Neel Nanda. Gemma Scope: Open Sparse Autoencoders Everywhere All At Once on Gemma 2, August 2024. URL http://arxiv.org/abs/2408.05147. arXiv:2408.05147 [cs].

Aleksandar Makelov. Sparse Autoencoders Match Supervised Features for Model Steering on the IOI Task. June 2024. URL https://openreview.net/forum?id=JdrVuEQih5.

Alireza Makhzani and Brendan Frey. k-Sparse Autoencoders, March 2014. URL http://arxiv.org/abs/1312.5663. arXiv:1312.5663 [cs].

Samuel Marks, Can Rager, Eric J. Michaud, Yonatan Belinkov, David Bau, and Aaron Mueller. Sparse Feature Circuits: Discovering and Editing Interpretable Causal Graphs in Language Models, March 2024. URL http://arxiv.org/abs/2403.19647. arXiv:2403.19647 [cs].

Andrew Ng. Sparse autoencoder, 2011. URL https://graphics.stanford.edu/courses/cs233-21-spring/ReferencedPapers/SAE.pdf.

nostalgebraist. Interpreting GPT: the logit lens, August 2020. URL https://www.lesswrong.com/posts/AcKRB8wDpdaN6v6ru/interpreting-gpt-the-logit-lens.

Chris Olah. The Next Five Hurdles, July 2024. URL https://transformer-circuits.pub/2024/july-update/index.html#hurdles.

Chris Olah, Nick Cammarata, Ludwig Schubert, Gabriel Goh, Michael Petrov, and Shan Carter. Zoom In: An Introduction to Circuits. *Distill*, 5(3), March 2020. ISSN 2476-0757. doi: 10.23915/distill.00024.001. URL https://distill.pub/2020/circuits/zoom-in.

Bruno A. Olshausen and David J. Field. Emergence of simple-cell receptive field properties by learning a sparse code for natural images. *Nature*, 381(6583):607–609, June 1996. ISSN 1476-4687. doi: 10.1038/381607a0. URL https://www.nature.com/articles/381607a0. Publisher: Nature Publishing Group.

Charles O'Neill and Thang Bui. Sparse Autoencoders Enable Scalable and Reliable Circuit Identification in Language Models, May 2024. URL http://arxiv.org/abs/2405.12522. arXiv:2405.12522 [cs].

Charles O'Neill, Christine Ye, Kartheik Iyer, and John F. Wu. Disentangling Dense Embeddings with Sparse Autoencoders, August 2024. URL http://arxiv.org/abs/2408.00657. arXiv:2408.00657 [cs].

Kiho Park, Yo Joong Choe, and Victor Veitch. The Linear Representation Hypothesis and the Geometry of Large Language Models, November 2023. URL http://arxiv.org/abs/2311.03658. arXiv:2311.03658 [cs, stat].

Alec Radford, Jeffrey Wu, Rewon Child, David Luan, Dario Amodei, and Ilya Sutskever. Language Models are Unsupervised Multitask Learners, 2019. URL https://cdn.openai.com/better-language-models/language_models_are_unsupervised_multitask_learners.pdf.

Senthooran Rajamanoharan, Arthur Conmy, Lewis Smith, Tom Lieberum, Vikrant Varma, Janos Kramar, Rohin Shah, and Neel Nanda. Improving Sparse Decomposition of Language Model Activations with Gated Sparse Autoencoders. June 2024a. URL https://openreview.net/forum?id=Ppj5KvzU8Q.

Senthooran Rajamanoharan, Tom Lieberum, Nicolas Sonnerat, Arthur Conmy, Vikrant Varma, János Kramár, and Neel Nanda. Jumping Ahead: Improving Reconstruction Fidelity with JumpReLU Sparse Autoencoders, July 2024b. URL http://arxiv.org/abs/2407.14435. arXiv:2407.14435 [cs].

Lee Sharkey, Dan Braun, and Beren Millidge. Taking features out of superposition with sparse autoencoders, December 2022. URL https://www.alignmentforum.org/posts/z6QQJbtpkEAX3Aojj/interim-research-report-taking-features-out-of-superposition.

Nishant Subramani, Nivedita Suresh, and Matthew Peters. Extracting Latent Steering Vectors from Pretrained Language Models. In Smaranda Muresan, Preslav Nakov, and Aline Villavicencio (eds.), *Findings of the Association for Computational Linguistics: ACL 2022*, pp. 566–581, Dublin, Ireland, May 2022. Association for Computational Linguistics. doi: 10.18653/v1/2022.findings-acl.48. URL https://aclanthology.org/2022.findings-acl.48.

Adly Templeton, Tom Conerly, Jonathan Marcus, Jack Lindsey, Trenton Bricken, Brian Chen, Adam Pearce, Craig Citro, Emmanuel Ameisen, Andy Jones, Hoagy Cunningham, Nicholas L. Turner, Callum McDougall, Monte MacDiarmid, Alex Tamkin, Esin Durmus, Tristan Hume, Francesco Mosconi, C. Daniel Freeman, Theodore R. Sumers, Edward Rees, Joshua Batson, Adam Jermyn, Shan Carter, Chris Olah, and Tom Henighan. Scaling Monosemanticity: Extracting Interpretable Features from Claude 3 Sonnet, May 2024. URL https://transformer-circuits.pub/2024/scaling-monosemanticity/index.html.

Lucrezia Valeriani, Diego Doimo, Francesca Cuturello, Alessandro Laio, Alessio Ansuini, and Alberto Cazzaniga. The geometry of hidden representations of large transformer models. *Advances in Neural Information Processing Systems*, 36:51234–51252, December 2023. URL https://proceedings.neurips.cc/paper_files/paper/2023/hash/a0e66093d7168b40246af1cddc025daa-Abstract-Conference.html.

Ashish Vaswani, Noam Shazeer, Niki Parmar, Jakob Uszkoreit, Llion Jones, Aidan N Gomez, Lukasz Kaiser, and Illia Polosukhin. Attention is All you Need. In *Advances in Neural Information Processing Systems*, volume 30. Curran Associates, Inc., 2017. URL https://papers.nips.cc/paper_files/paper/2017/hash/3f5ee243547dee91fbd053c1c4a845aa-Abstract.html.

Kevin Wang, Alexandre Variengien, Arthur Conmy, Buck Shlegeris, and Jacob Steinhardt. Interpretability in the Wild: a Circuit for Indirect Object Identification in GPT-2 small, November 2022. URL http://arxiv.org/abs/2211.00593. arXiv:2211.00593 [cs].

Martin Wattenberg and Fernanda Viégas. Relational Composition in Neural Networks: A Survey and Call to Action. June 2024. URL https://openreview.net/forum?id=zzCEiUIPk9.

James C. R. Whittington, Will Dorrell, Surya Ganguli, and Timothy E. J. Behrens. Disentanglement with Biological Constraints: A Theory of Functional Cell Types, March 2023. URL http://arxiv.org/abs/2210.01768. arXiv:2210.01768 [cs, q-bio].

John Wright and Yi Ma. *High-Dimensional Data Analysis with Low-Dimensional Models: Principles, Computation, and Applications*. Cambridge University Press, 1 edition, January 2022. ISBN 978-1-108-77930-2 978-1-108-48973-7. doi: 10.1017/9781108779302. URL https://www.cambridge.org/highereducation/product/9781108779302/book.

Zeyu Yun, Yubei Chen, Bruno Olshausen, and Yann LeCun. Transformer visualization via dictionary learning: contextualized embedding as a linear superposition of transformer factors. In Eneko Agirre, Marianna Apidianaki, and Ivan Vulić (eds.), *Proceedings of Deep Learning Inside Out (DeeLIO): The 2nd Workshop on Knowledge Extraction and Integration for Deep Learning Architectures*, pp. 1–10, Online, June 2021. Association for Computational Linguistics. doi: 10.18653/v1/2021.deelio-1.1. URL https://aclanthology.org/2021.deelio-1.1.

A Training

We train each autoencoder on 1 billion tokens from the Pile (Gao et al., 2020), excluding the copyrighted Books3 dataset,[2] for a single epoch. Specifically, we concatenate a batch of 1024 text samples with the end-of-sentence token, tokenize the concatenated text, and divide the output into sequences of 2048 tokens, discarding the final incomplete sequence. We use an effective batch size of 131072 tokens (64 sequences) for all experiments.

We do not compute activation vectors and cache them to disk before training, which minimizes storage overhead at the expense of repeated computation. Following Lieberum et al. (2024), we exclude activation vectors corresponding to special tokens (end-of-sentence, beginning-of-sentence, and padding) from the inputs to the autoencoder. The total number of activation vectors is the number of non-special tokens multiplied by the number of layers.

Following the optimization guidelines in Bricken et al. (2023); Gao et al. (2024), we initialize the pre-encoder bias $\mathbf{b}_{\text{pre}}$ to the geometric median of the first training batch; we initialize the decoder weight matrix $\mathbf{W}_{\text{dec}}$ to the transpose of the encoder $\mathbf{W}_{\text{enc}}$; we scale the decoder weight vectors to unit norm at initialization and after each training step; and we remove the component of the gradient of the decoder weight matrix parallel to its weight vectors after each training step.

We use the Adam optimizer (Kingma & Ba, 2017) with the default β parameters, a constant learning rate of 1×10^{-4}, and $\epsilon = 6.25 \times 10^{-10}$. Unlike Gao et al. (2024), we do not use gradient clipping or weight averaging, and we use FP16 mixed precision to reduce memory use.

B Tuned lens

The 'logit lens' is a method to interpret directions in the residual stream by projecting them onto the vocabulary space to elicit token predictions, i.e., multiplying them by the unembedding matrix (nostalgebraist, 2020). However, the residual stream basis is not fixed, so Belrose et al. (2023) introduce the 'tuned lens' approach, where a linear transformation is learned for each layer in the residual stream. The objective is to minimize the KL divergence between the probability distribution over tokens generated by the transformed activations and the 'true' distribution of the model. This approach draws on the perspective of iterative inference (Jastrzębski et al., 2018).

B.1 Method

In the tuned lens method, an affine transformation is learned from the output space of layer ℓ to the output space of the final layer, called the translator for layer ℓ (Belrose et al., 2023). With our setup, we want to transform the residual stream activation vectors at each layer into more similar bases before passing them to the encoder and invert that transformation after the decoder.

Importantly, the authors note that their implementation[3] uses a residual connection:

$$\mathbf{x}' = \mathbf{x} + (\mathbf{W}_{\text{lens}}\mathbf{x} + \mathbf{b}_{\text{lens}}) \tag{9}$$

Here, $\mathbf{x}$ is the input vector to the encoder, and $\mathbf{x}'$ is the transformed input vector. This parameterization ensures that L_2 regularization (weight decay) pushes the transformation towards the identity matrix instead of zero. Hence, to invert the transformation, we need:

$$\hat{\mathbf{x}} = (\mathbf{I} + \mathbf{W}_{\text{lens}})^{-1}(\hat{\mathbf{x}}' - \mathbf{b}_{\text{lens}}) \tag{10}$$

Here, $\hat{\mathbf{x}}'$ is the transformed output vector of the decoder, $\hat{\mathbf{x}}$ is the output vector, $\mathbf{W}_{\text{lens}} \in \mathbb{R}^{d \times d}$, and $\mathbf{b}_{\text{lens}} \in \mathbb{R}^{d}$. With our setup, $\mathbf{x}'$ and $\hat{\mathbf{x}}'$ replace the input and output vectors that we pass to the encoder and use to compute the loss (Section 3). Notably, we use the transformed vectors to compute reconstruction errors (Figure 12). We compute the inverse $(\mathbf{I} + \mathbf{W}_{\text{lens}})^{-1}$ for each layer once at the start of training.

We use pre-trained tuned lenses provided by the authors of Belrose et al. (2023). Notably, these did not include Pythia-1b at the time of writing.[4]

[2] `https://huggingface.co/datasets/monology/pile-uncopyrighted`

[3] `https://github.com/AlignmentResearch/tuned-lens`, file: `tuned_lens/nn/lenses.py`

[4] `https://huggingface.co/spaces/AlignmentResearch/tuned-lens`

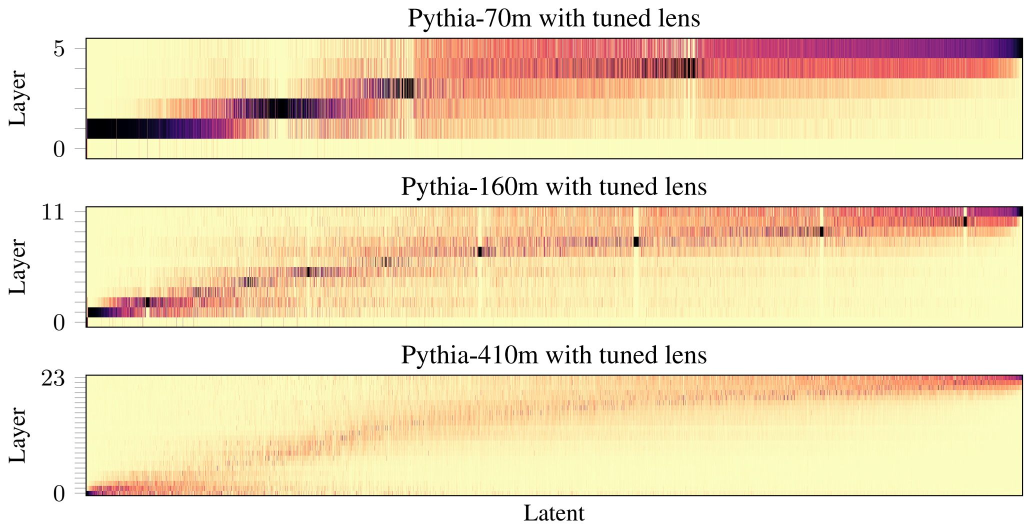

Figure 6: Heatmaps of the distributions of latent activations over layers when aggregating over 10 million tokens from the test set. Here, we plot the distributions for tuned-lens MLSAEs trained on Pythia models with an expansion factor of $R = 64$ and sparsity $k = 32$. For standard MLSAEs, see Figure 2. We note that a pre-trained tuned lens was not available for Pythia-1b.

B.2 Results

We had expected that tuned-lens transformations would increase the degree to which latents were active at multiple layers because they translate the activations at every layer into a basis more similar to the basis of the output layer. The aggregate and single-prompt heatmaps (Figures 6 and 7) indicate a modest increase in the degree to which latents are active at multiple layers compared with the standard approach.

The variance ratios in Figure 16 clarify that the tuned-lens approach decreases the degree to which latents are active at multiple layers when aggregating over tokens. This ratio remains approximately constant as the expansion factor increases (between 37% and 41%). Conversely, the variances for a single token relative to a single latent are larger, i.e., the single-prompt heatmaps are more 'spread out' compared with the standard approach, except for Pythia-410m (Figure 16).

C Evaluation

The key advantage of a multi-layer SAE is to be able to study how information flows across layers in the residual stream. However, this approach is only useful if the MLSAE performs comparably to single-layer SAEs. Table 1 summarizes the evaluation results for MLSAEs trained on Pythia models with our default hyperparameters. The FVU, delta cross-entropy (CE) loss, and KL divergence remain consistent across model sizes. In most cases, applying tuned-lens transformations decreases the FVU and delta CE loss but not the KL divergence (Figure 12).

C.1 Reconstruction error and sparsity

While we use the FVU instead of MSE as the reconstruction error in the training loss, we record both metrics for the inputs from each transformer layer and the mean over all layers (Figure 8). The L^0 norm of the latents is fixed at k per activation vector (layer and token), but we record the L^1 norm (Figure 9). We report the values of these metrics over one million tokens from the test set.

For Pythia-70m, the FVU at each layer is comparable to Marks et al. (2024, p. 21), who trained separate SAEs with $n = 32768$ and L^0 norms between 54 and 108, as well as Cunningham et al. (2023, p. 13). For Pythia-160m, the FVU is similar to Gao et al. (2024), who report the normalized MSE on layer 8 of GPT-2 small.

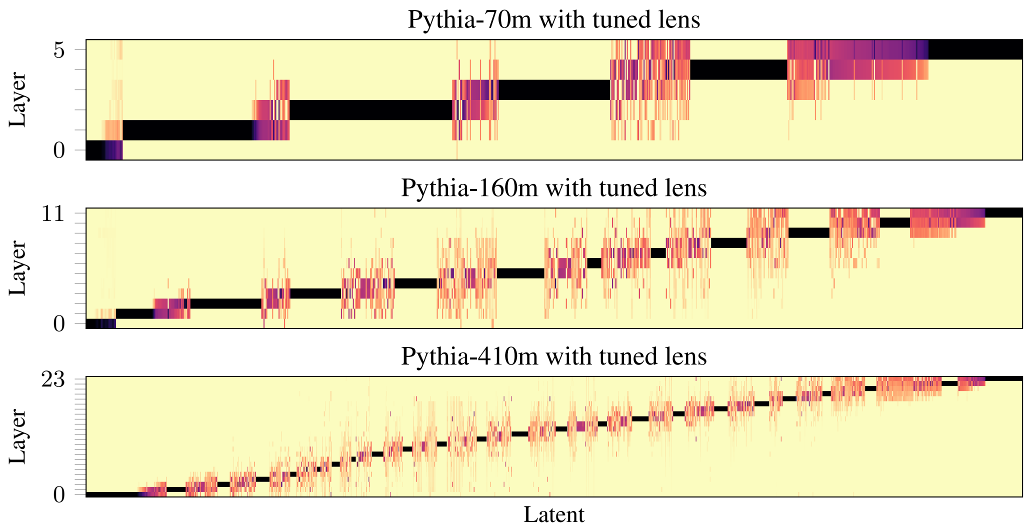

Figure 7: Heatmaps of the distributions of latent activations over layers for a single example prompt. Here, we plot the distributions for tuned-lens MLSAEs trained on Pythia models with an expansion factor of $R = 64$ and sparsity $k = 32$. The example prompt is "When John and Mary went to the store, John gave" (Wang et al., 2022). For standard MLSAEs, see Figure 3. We note that a pre-trained tuned lens was not available for Pythia-1b.

Model	Pythia-70m	Pythia-160m	Pythia-410m	Pythia-1b	GPT-2 small
FVU	0.097	0.106	0.827	0.095	0.093
MSE	0.103	0.105	1.400	0.455	5.782
L1 Norm	66	76	96	110	197
Delta CE Loss	0.565	0.432	6.973	0.404	0.759
KL Divergence	$1.621 \cdot 10^3$	$1.217 \cdot 10^3$	$1.801 \cdot 10^4$	$1.057 \cdot 10^3$	$1.023 \cdot 10^3$

(a) Standard

Model	Pythia-70m	Pythia-160m	Pythia-410m
FVU	0.030	0.088	0.073
MSE	0.838	0.404	0.133
L1 Norm	61	90	80
Delta CE Loss	0.274	-0.080	0.827
KL Divergence	$2.718 \cdot 10^3$	$1.962 \cdot 10^3$	$1.448 \cdot 10^3$

(b) Tuned lens

Table 1: The mean reconstruction errors and downstream loss metrics for MLSAEs with an expansion factor of $R = 64$ and sparsity $k = 32$, over 1 million tokens from the test set.

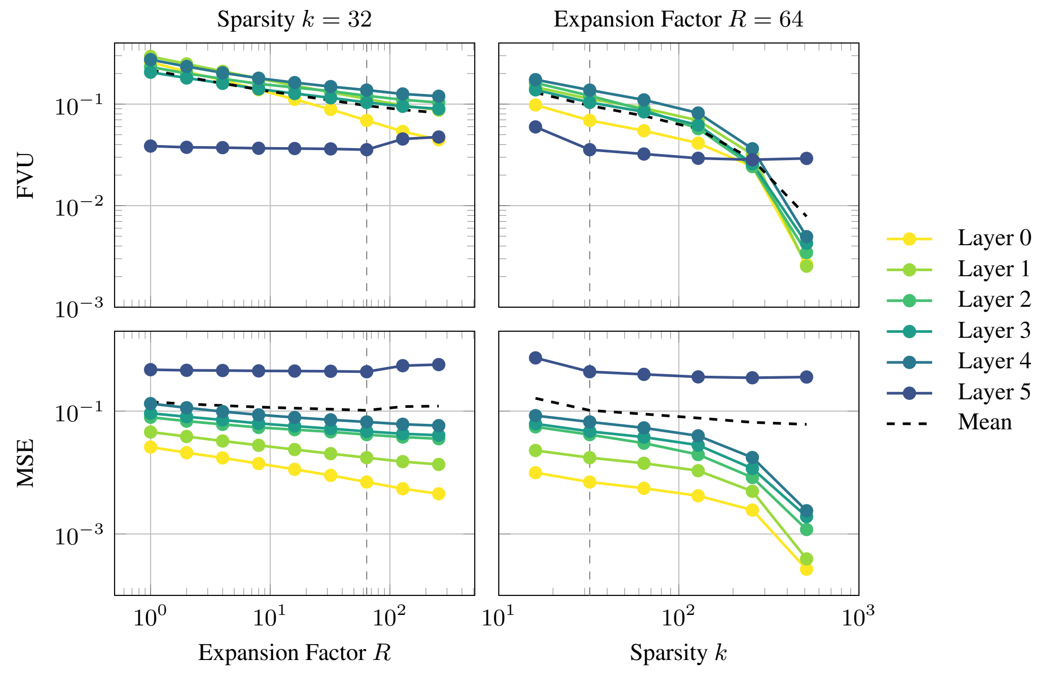

(a) Pythia-70m

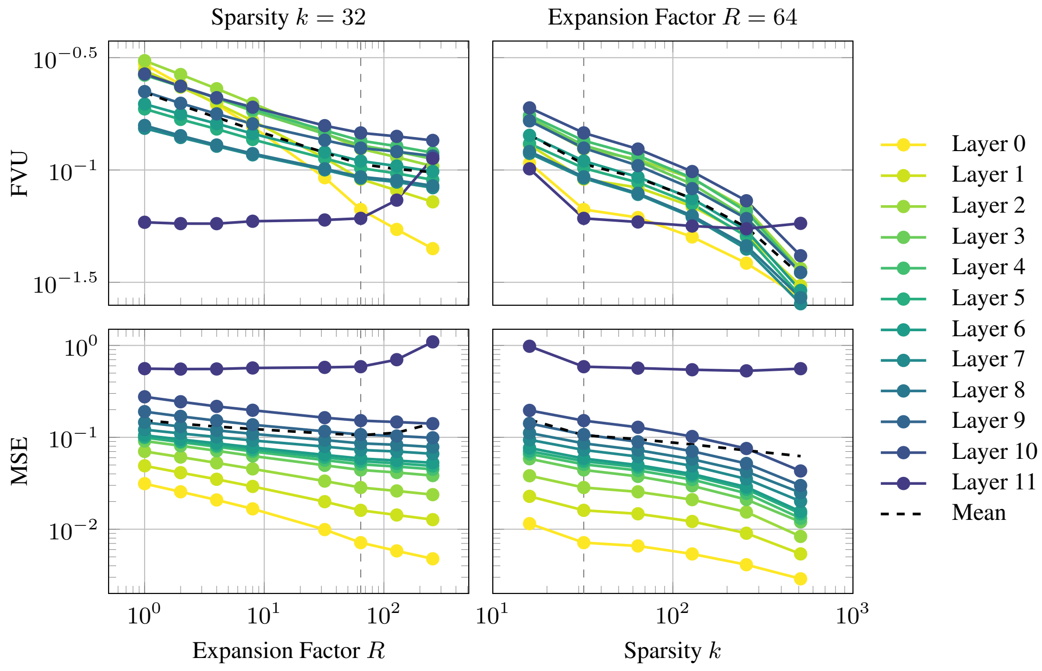

(b) Pythia-160m

Figure 8: With fixed sparsity $k = 32$, the FVU and MSE generally decrease as the expansion factor R increases. For inputs from the last layer, they increase for the largest expansion factors, which we attribute to fluctuations in the percentage of dead latents (Figure 11). With fixed expansion factor $R = 64$, the FVU and MSE decrease as the sparsity k increases. While all inputs are standardized before passing them to the encoder, the decoder outputs are rescaled afterward. Hence, the MSE increases across layers because it is not divided by the variance of the inputs.

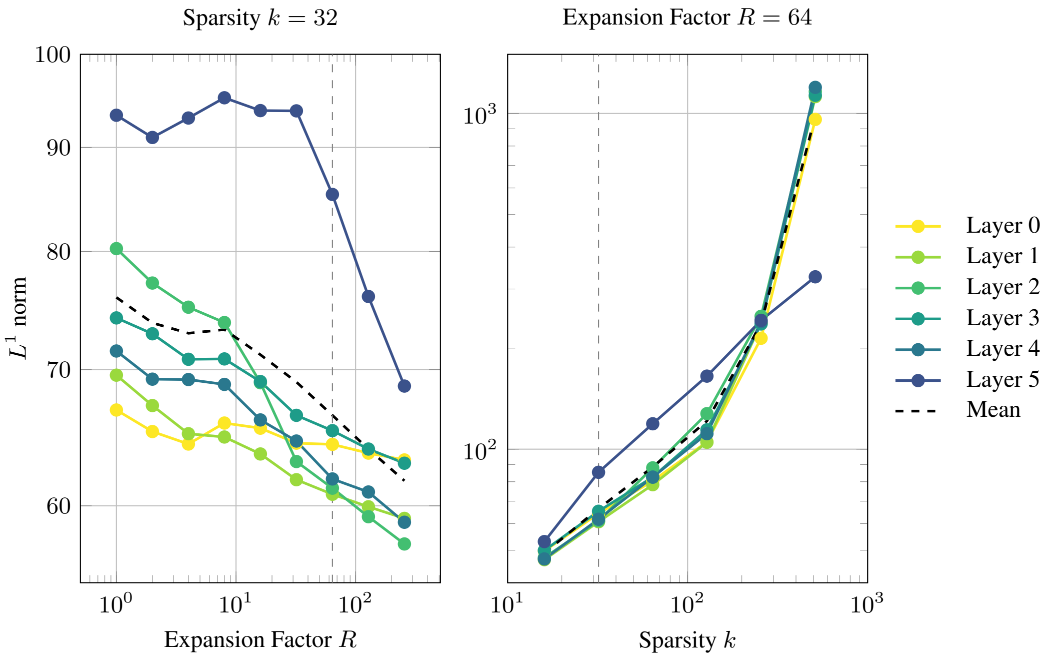

(a) Pythia-70m

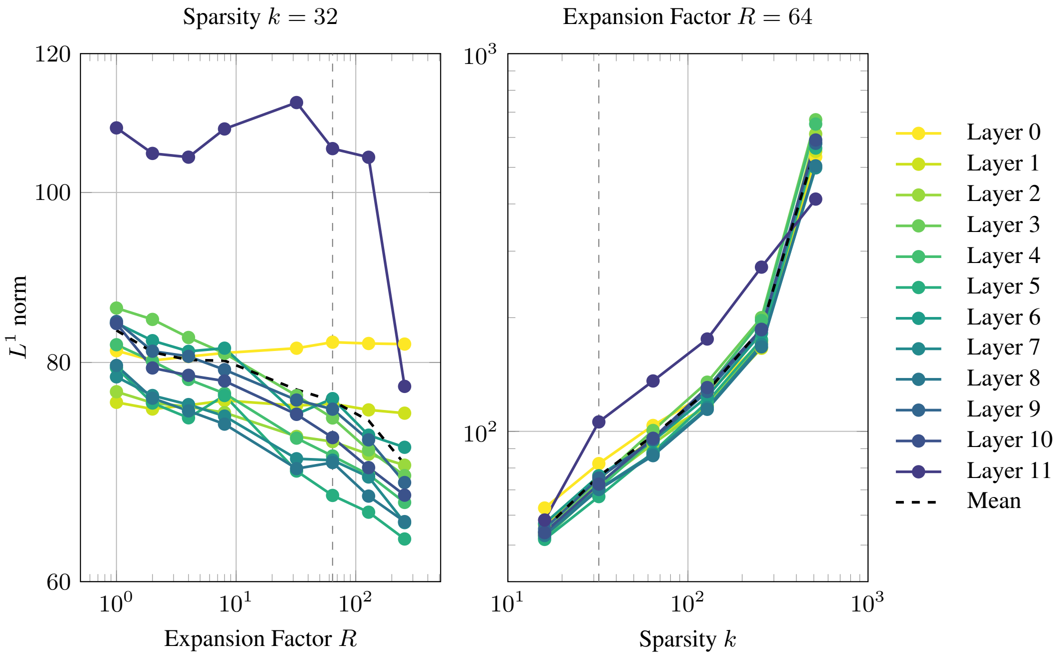

(b) Pythia-160m

Figure 9: With fixed sparsity $k = 32$, the L^1 norm per token (the sum of absolute activations) generally decreases as the expansion factor R increases. With fixed expansion factor $R = 64$, the L^1 norm increases as the sparsity k increases. Recall that the L^0 norm per token (the count of non-zero activations) is fixed at k.

Model	Mean	Std. Dev.
Pythia-70m	0.275	0.0843
Pythia-160m	0.250	0.0928
Pythia-410m	0.221	0.0868
Pythia-1b	0.201	0.0989
GPT-2 small	0.258	0.0703

(a) Standard

Model	Mean	Std. Dev.
Pythia-70m	0.261	0.0763
Pythia-160m	0.206	0.0734
Pythia-410m	0.216	0.0864

(b) Tuned lens

Table 2: The mean and standard deviation of the maximum cosine similarity between decoder weight vectors. Here, we report the MMCS for MLSAEs with an expansion factor of $R = 64$ and sparsity $k = 32$. Recall that GPT-2 small is similar in size to Pythia-160m.

C.2 Downstream loss

The reconstruction error is a proxy for the degree to which an autoencoder explains the behavior of the underlying transformer. Hence, we also measure the change in transformer outputs when the residual stream activations at a given layer are replaced by their reconstruction. Following Braun et al. (2024); Gao et al. (2024); Lieberum et al. (2024), we record the increase in cross-entropy (CE) loss and the Kullback-Leibler (KL) divergence between probability distributions. We report the values of these metrics over one million tokens from the test set (Figure 10).

The increase in cross-entropy loss is comparable to Marks et al. (2024, p. 21) for Pythia-70m, Gao et al. (2024, p. 5) and Braun et al. (2024) for GPT-2 small, and Lieberum et al. (2024, p. 7-8) for layer 20 of Gemma 2 2B and 9B.

C.3 Comparison with GPT-2

We predominantly study GPT-style models from the Pythia suite (Biderman et al., 2023). While we do not expect our results to depend strongly on the underlying transformer architecture, we also trained an MLSAE on GPT-2 small (Radford et al., 2019) with our default hyperparameters. We include quantitative results for GPT-2 small in Table 1, Table 2, Figure 15, and Figure 16; and aggregate and single-prompt heatmaps of the distributions of latent activations over layers in Figures 13 and 14. We note that GPT-2 small is similar in size to Pythia-160m.

D Mean max cosine similarity

Sharkey et al. (2022) define the Mean Max Cosine Similarity (MMCS) between a learned dictionary X and a ground-truth dictionary X'. There is no ground-truth dictionary for language models, so a larger learned dictionary or the k nearest neighbors to each dictionary element are commonly used.

$$\text{MMCS}(X, X') = \frac{1}{|X|} \sum_{\mathbf{x} \in X} \max_{\mathbf{x}' \in X'} \cos \text{sim}(\mathbf{x}, \mathbf{x}') \tag{11}$$

The MMCS serves as a proxy measure for 'feature splitting' (Bricken et al., 2023; Braun et al., 2024): as the number of features increases, we expect the decoder weight vectors to be more similar to their nearest neighbors. We compute the MMCS with $k = 1$ after training, finding it decreases slightly as the model size increases with fixed hyperparameters (Table 2).

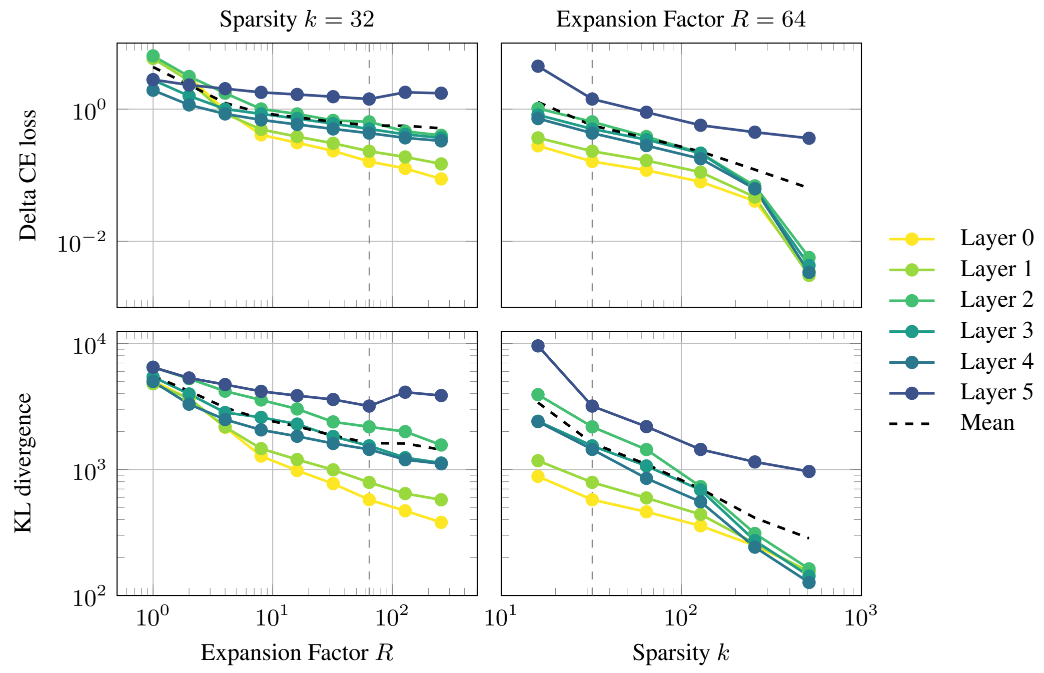

(a) Pythia-70m

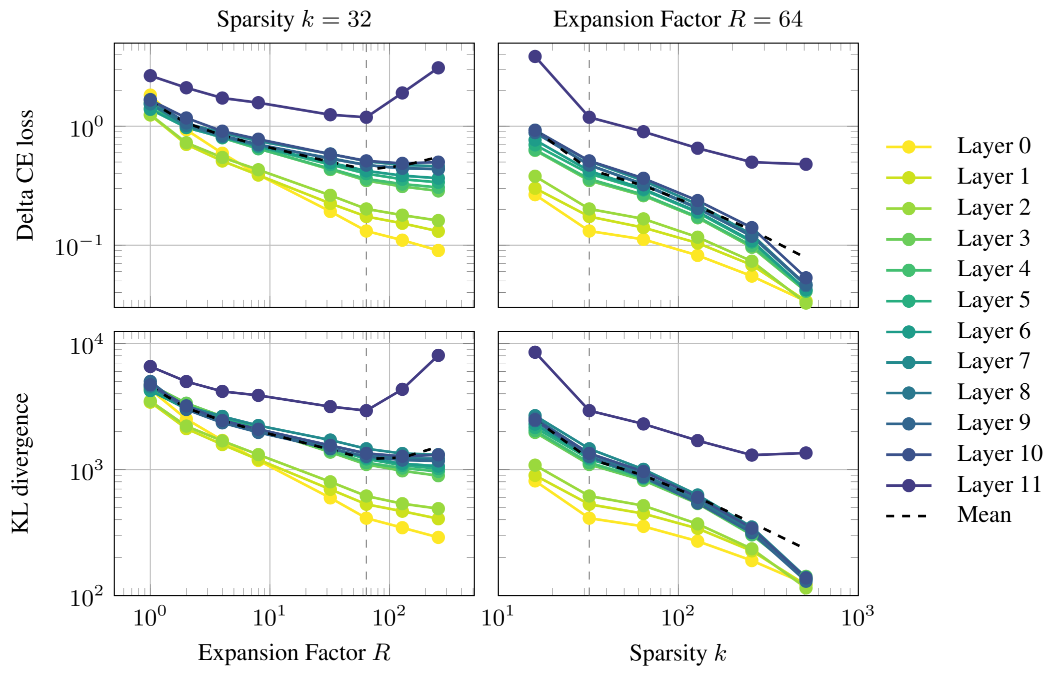

(b) Pythia-160m

Figure 10: With fixed sparsity $k = 32$, the delta CE loss and KL divergence generally decrease as the expansion factor increases, except for inputs from the last layer. With fixed expansion factor $R = 64$, both metrics decrease as the sparsity k increases, similarly to the FVU and MSE (Figure 8).

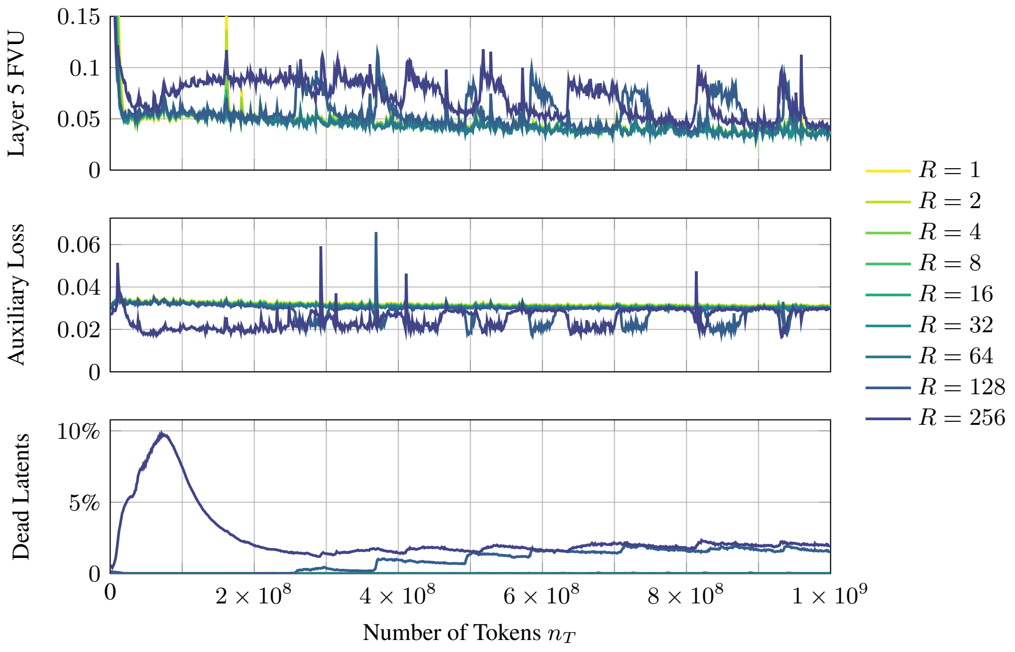

Figure 11: An illustration of the FVU for inputs from the last layer, compared to the auxiliary loss and percentage of dead latents, for MLSAEs trained on Pythia-70m with fixed sparsity $k = 32$. An increase in dead latents correlates with a decrease in the auxiliary loss and an increase in the FVU at the last layer. We attribute this to the increased scale of the inputs because the auxiliary loss depends on the MSE (Figure 8). The auxiliary loss is multiplied by its coefficient $\alpha = {}^1\!/_{32}$ in the training loss.

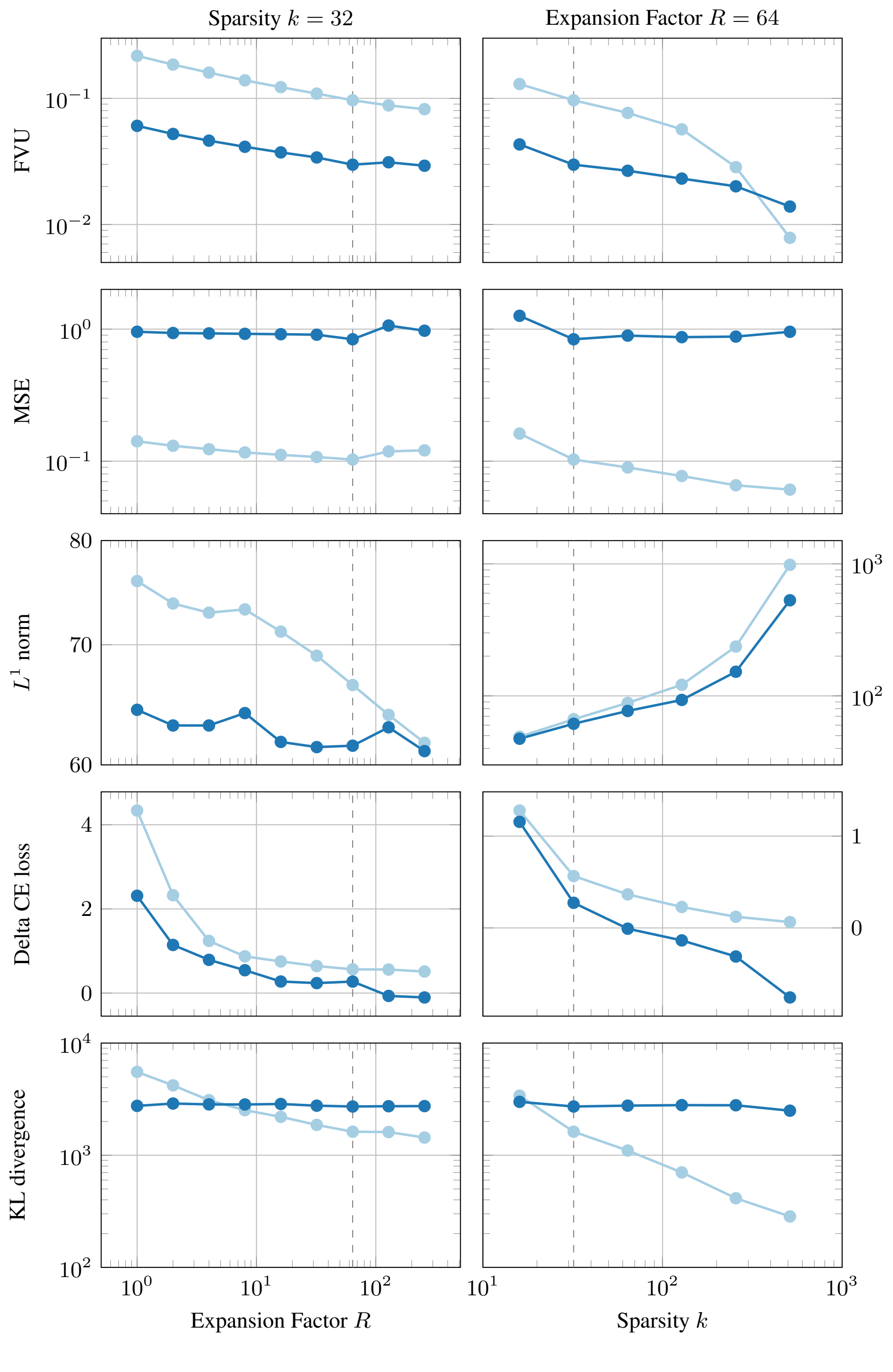

Figure 12: For Pythia-70m, applying tuned-lens transformations decreases the mean FVU and delta cross-entropy loss but not the KL divergence. Importantly, we compute reconstruction errors before applying the inverse transformation and downstream loss metrics afterward (Appendix B.1). Unlike Figure 10, we use a linear scale for the delta cross-entropy loss because, surprisingly, it is negative for tuned-lens MLSAEs with a large expansion factor R or sparsity k.

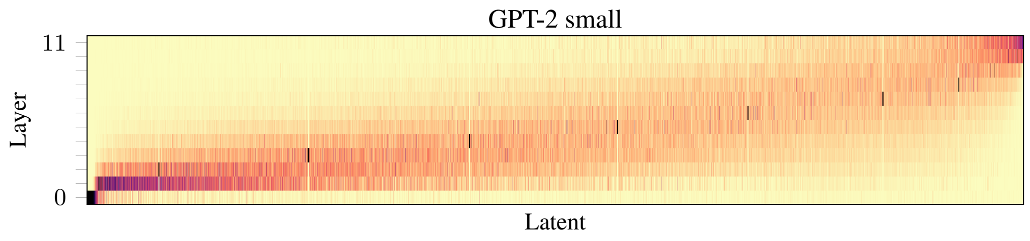

Figure 13: Heatmaps of the distributions of latent activations over layers when aggregating over 10 million tokens from the test set. Here, we plot the distributions for an MLSAE trained on GPT-2 small with an expansion factor of $R = 64$ and sparsity $k = 32$. We provide further details in Figure 2.

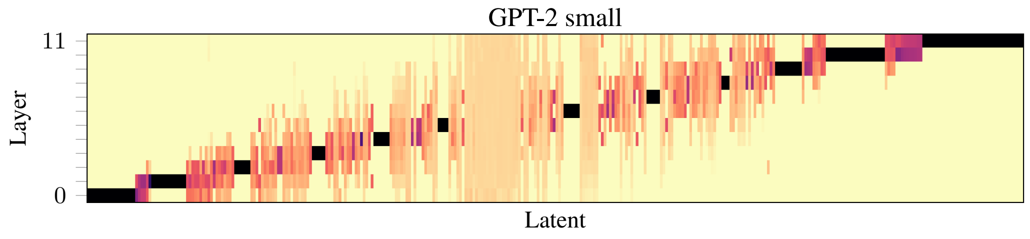

Figure 14: Heatmaps of the distributions of latent activations over layers for a single example prompt. Here, we plot the distributions for an MLSAE trained on GPT-2 small with an expansion factor of $R = 64$ and sparsity $k = 32$. The example prompt is “When John and Mary went to the store, John gave” (Wang et al., 2022). We provide further details in Figure 3.

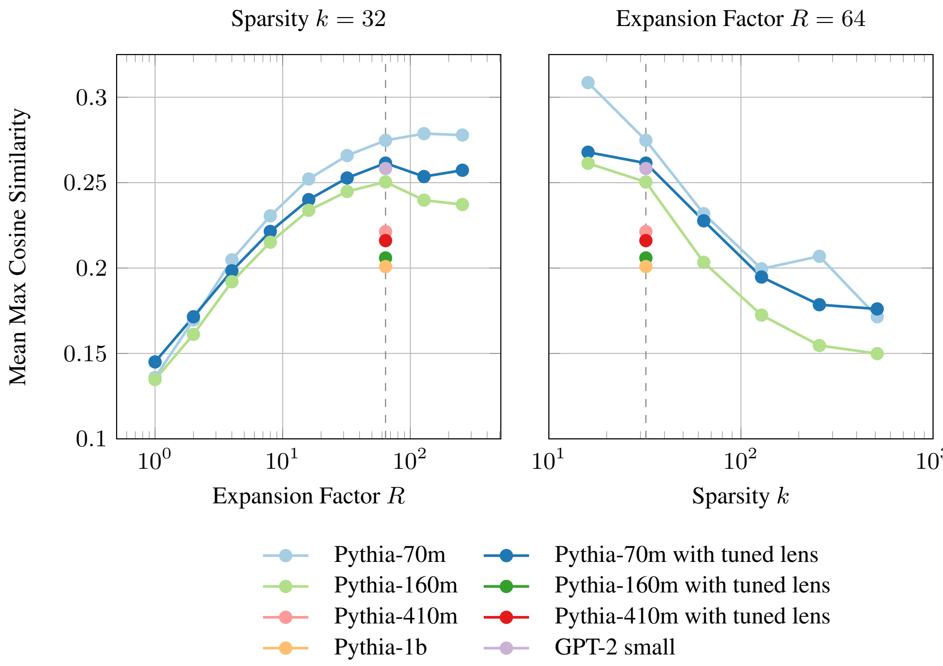

Figure 15: The Mean Max Cosine Similarity for standard and tuned-lens MLSAEs (Eq. 11). Generally, the MMCS increases as the expansion factor R increases and decreases as the sparsity k increases, and applying tuned-lens transformations slightly decreases the MMCS.

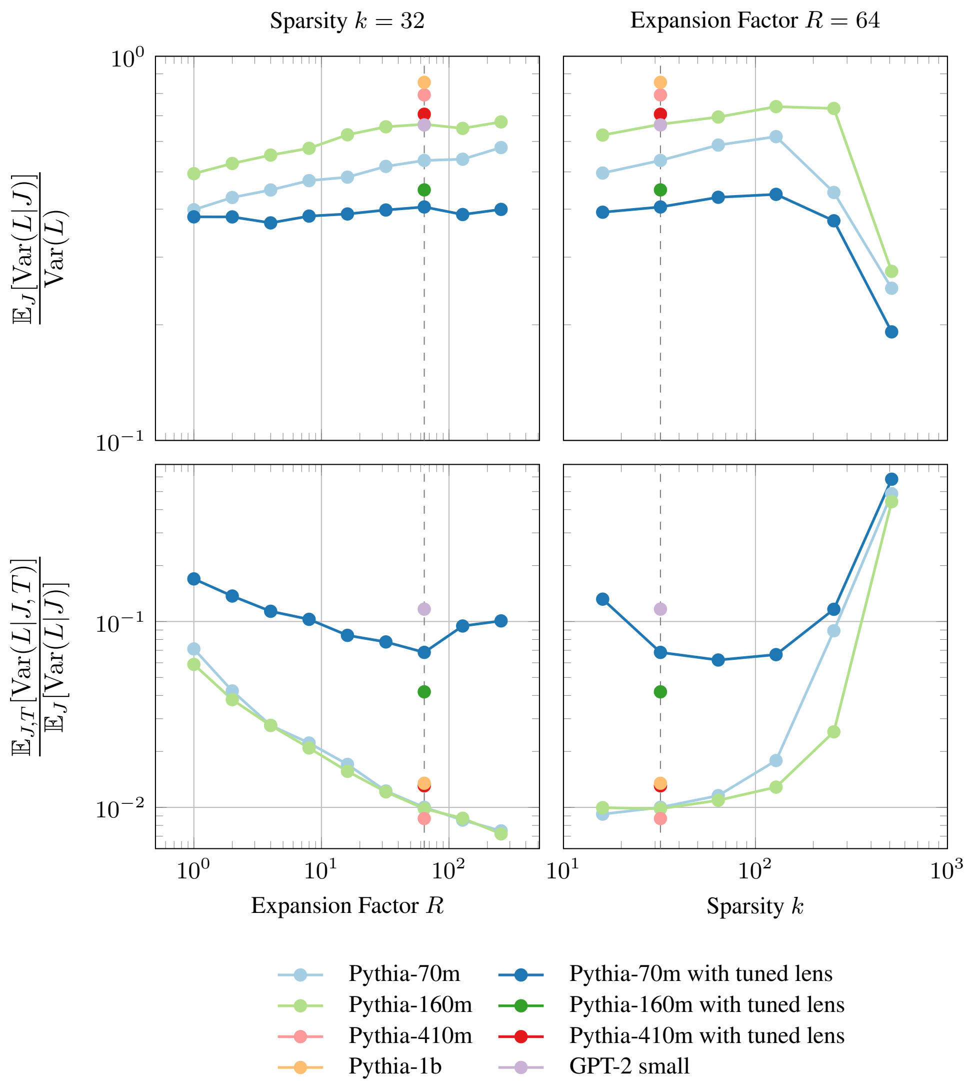

Figure 16: The fraction of the total variance explained by individual latents and the fraction of the variance for an individual latent explained by individual tokens (Eqs. 7 and 8). Here, we plot the variance ratios for standard and tuned-lens MLSAEs over 10 million tokens from the test set.